

Taxonomy of Power Converter Control Schemes based on the Complex Frequency Concept

Dionysios Moutvelis, Javier Roldán-Pérez, *Member, IEEE*
Milan Prodanovic *Member, IEEE*, and Federico Milano, *Fellow, IEEE*

Abstract—This paper proposes a taxonomy of power converter control schemes based on the recently proposed concept of *complex frequency*. This quantity captures local frequency variations due to the change of both the phase angle and amplitude of bus voltages and current injections. The paper derives the analytical expressions of the link between complex power variations and complex frequency of each converter controller as well as the identification of critical control parameters. The main contribution of this work is to provide a general framework that allows classifying converters synchronization mechanisms and controllers. This framework also allows comparing converters with synchronous machines. To validate the theoretical results, extensive simulations are performed using a modified version of the WSCC 9-bus system. Examples of how the theoretical formulations of the paper can be used to improve power converter control in power system applications are showcased.

Index Terms—Complex frequency, grid-following, grid-forming, power converter, synchronization, frequency control.

I. INTRODUCTION

A. Motivations

The high penetration of converter-interfaced energy resources in modern power grids makes necessary the contribution of these devices to the frequency regulation of the network [1]. A variety of such converter-based, frequency regulating strategies has been proposed in the literature [2, 3]. The stability and transient operation of these controllers is well studied and documented [2, 4]. However, the contribution of each controller to the frequency at the converter connection point has not been yet fully discussed. In this paper, the recently proposed concept of Complex Frequency (CF) is employed to fill precisely this gap and discuss, through a rigorous analytical appraisal, the effect of different power converter controllers on the frequency at the converter connection bus. The results are organized in a systematic taxonomy of power converter synchronization and control schemes.

D. Moutvelis, J. Roldán-Pérez, and M. Prodanovic are with the Electrical Systems Unit, IMDEA Energy, Avda. Ramón de la Sagra 3, 28935, Móstoles, Madrid, Spain. E-mail: dionysios.moutvelis@imdea.org, javier.rolan@imdea.org, milan.prodanovic@imdea.org. D. Moutvelis is also with Alcalá de Henares University, Alcalá de Henares 28801 Madrid, Spain. F. Milano is with School of Electrical and Electronic Engineering, University College Dublin, Belfield Campus, Dublin 4, D04V1W8, Ireland. E-mail: federico.milano@ucd.ie

This work is partly supported by the Community of Madrid, research project PROMINT-CM (P2018/EMT4366), and Juan de la Cierva Incorporación program (IJC2019-042342-I) from the Spanish Government by funding D. Moutvelis, J. Roldán-Pérez, and M. Prodanovic and by the Sustainable Energy Authority of Ireland (SEAI) by funding F. Milano under project FRESLIPS, Grant No. RDD/00681.

B. Literature Review

Converter control schemes are commonly grouped into the Grid-Following (GFL) or Grid-Forming (GFM) categories [5, 6]. The former are meant to measure or estimate the frequency of the grid while passively injecting the power that is requested from them. The synchronization is usually achieved by means of a Phase-Locked Loop (PLL) device [4, 6]. Extensive research regarding PLL stability and synchronization capability, especially in weak grids, has been carried out [7, 8]. However, GFL converters with PLLs are commonly assumed to not affect the frequency at their connection point. GFM converters do not rely on measuring or estimating the grid voltage. Instead, they achieve synchronization with the grid by varying the active power injection [4]. Various power-based synchronization strategies can be found in the literature [2–4]. Although the optimal GFM control method is still an open research field, the most common ones found both in the literature and in practical applications are the *droop control* and the *Virtual Synchronous Machine (VSM)* [9–13]. Droop controlled converters adjust their active power output through an active power-frequency (P/f) droop rule to achieve synchronization [9, 10]. VSM-based converters fully emulate a swing equation within their control structure, typically of second order [11–13]. Many VSM implementations exist with all recent works highlighting the necessity of inner current and voltage controllers in a cascaded configuration [14]. These cascaded loops allow the explicit inclusion of voltage and current limitations that are necessary for the safe operation of the converters [15]. Moreover, dedicated voltage control loops are required for the operation of the converter as a voltage source [4]. It is thus of interest to quantify the effect of all these internal (current, voltage, PLL) and external (droops, VSM) controllers on the frequency at the converter ac bus.

The precise definition of the frequency of a power system is an open research topic which has recently received renewed attention [16]. In [17], the point was raised that frequency is not uniform in the whole network, especially in transient conditions, and a formula to estimate the frequency at each system bus is proposed. In [18], the concept of CF is proposed as an extension of the well-known definition of frequency as the time derivative of the argument of a sinusoidal signal [19]. This complex variable quantifies the change of the network frequency caused by the variation of both the phase angle and the magnitude of the voltage. The interpretation of CF is approached in the literature from various viewpoints [20]. The imaginary part of the frequency is, in effect, the conventional

quantity that is commonly utilized, in signal processing and time-frequency analysis, to define the *instantaneous frequency* of a signal. Using the same signal processing approach, the real part of the frequency can be defined as *instantaneous bandwidth* [21]. The geometric approach, presented in [22], assumes that the voltage (current) is *the speed of a trajectory in space*. This is supported by the fact that the voltage (current) is the time derivative of a time-varying flux (electric charge). This approach leads to define the real and imaginary parts of the CF as the symmetrical and anti-symmetrical components, respectively, of the time derivative of the voltage (current). Finally, in [23], based again on the analogy between voltage (current) and the speed of a trajectory, the real part of the CF is interpreted as a *radial speed*, whereas the imaginary part is interpreted as an *azimuthal speed*.

CF has been utilized to develop novel approaches in power system state estimation [24] as well as to study the synchronization stability of converters using dispatchable virtual oscillator control [25,26]. However, the various converter control schemes that are found in the literature have not been studied, thus far, under the lens of CF. This paper aims at filling this gap. In [27], the magnitude of the complex frequency was utilized as a metric to compare the performance of converter primary frequency and voltage controllers. In the same spirit, the present work is an application of the concept of complex frequency to the characterization of the dynamic behavior of the different parts that form the synchronization of the control of power electronics converters.

C. Contributions

The contributions of this paper are summarized as follows:

- The notion of voltage CF presented in [18] is extended to other variables and signals. It is explained how CF can be used as derivative operator for these signals, e.g., currents or voltage references.
- Then, the generalised CF quantity, i.e. resulting from the extension above, is used to derive the effect of different converter control schemes on the grid frequency. This novel approach allows the decoupling of the effect of different participating controllers and the identification of critical control parameters. These parameters can then be tuned appropriately to maximize or minimize the controller effect on the grid frequency.
- The local frequency as perceived by the converter is calculated and categorized. This *internal* frequency differs from the bus frequency due to the action of the converter controllers and synchronization mechanism. A parallel with the rotor speed of a synchronous machine is drawn, allowing the study of the two generation types (synchronous and asynchronous) using the same theoretical tools. Examples of how the internal frequency can be used to improve converter control are included.

The theoretical contributions of this work are supported by extended simulations taking into account various controller configurations, both GFL and GFM, and the operation of a realistic grid benchmark.

D. Paper Organization

The organization of the rest of the paper is as follows. In Section II, the theoretical framework for the use of CF as a derivative operator is established. In Section III, some general mathematical derivations that establish the relationship between frequency and complex power are presented. Then, they are used to define some common special cases in power systems as well as to analyze the fundamental current controller of power converters. Sections IV and V present the effect on CF of GFL and GFM control schemes, respectively. Section VI validates the theoretical results with a case study based on the modified WSCC 9-bus system. Lastly, Section VII draws conclusions and outlines future work.

II. COMPLEX FREQUENCY AS A DERIVATIVE OPERATOR

As it is well known, a complex quantity \bar{u} can be written either in polar or rectangular coordinates, as follows:

$$\bar{u} = u_d + j u_q = u \exp(j\varphi), \quad (1)$$

where $u = \sqrt{u_d^2 + u_q^2}$ and $\varphi = \arctan(u_q/u_d)$. For $u \neq 0$, the polar form can be also written as:

$$\bar{u} = \exp(\ln(u) + j\varphi). \quad (2)$$

Throughout this paper, the annotation from (1) will be used to signify all complex quantities referred to a dq-axis reference frame, including currents, voltages, control signals etc. The time derivative of (2) gives:

$$\dot{\bar{u}} = (\dot{u}/u + j\dot{\varphi}) \bar{u} = (\rho_u + j\omega_u) \bar{u} = \bar{\eta}_u \bar{u}. \quad (3)$$

The quantity $\bar{\eta}_u$ has been utilized in [18] to define the concept of CF of time-dependent Park vectors of the voltage and of the injected current at a bus h , as follows:

$$\dot{\bar{v}}_h = \bar{\eta}_v \bar{v}_h, \quad \dot{\bar{i}}_h = \bar{\eta}_i \bar{i}_h. \quad (4)$$

The CF includes a real part, which represents a *translation* and depends only on the magnitude of the Park vector; and an imaginary part, which represents a *rotation* and depends only on the phase angle of the Park vector. These two quantities can be viewed as a special case of the symmetric and anti-symmetric components of the more general concept of geometric frequency defined in [22]. The advantage of defining the real part of the CF is twofold: (i) it provides a quantity that has the same transient nature and same units as the conventional instantaneous frequency, and is thus directly comparable to it; and (ii) it allows a consistent description and formulation of the dynamic effect of the devices that are connected to the grid.

Note that, in general and in transient conditions, $\bar{\eta}_v \neq \bar{\eta}_i$, as discussed in [18]. Moreover, note that quantities $\bar{\eta}_v$ and $\bar{\eta}_i$ represent the variations of voltage and current frequency, respectively, from the nominal, steady-state values $\bar{\eta}_{vn} = \bar{\eta}_{in} = 0 + j\omega_n$, where $\omega_n = 2\pi f_n$ is the nominal frequency of the grid.

The rotation of the dq-axis coordinates has an important effect on the CF if this rotation is time dependent. Relevantly, this is the case of synchronous machines [18], and converters

that are synchronized to the grid by means of a synchronization control strategy (active power synchronization for GFM converters [9, 15], or PLL for GFL converters [4, 6]). The rotation from the local to the grid reference frame can be written as:

$$\bar{v}_h = \exp(j\delta) \bar{v}'_h, \quad \bar{i}_h = \exp(j\delta) \bar{i}'_h, \quad (5)$$

where ' denotes variables in the local (i.e., device-side) reference frame and δ is the angle variation between the two reference frames. For example, in the case of the synchronous machine, δ refers to the transformation from the rotor reference frame to the stator while for the case of converters, it transforms quantities from the converter reference frame to the network reference frame using the angle of the controller. Note that the rotation (5) is power invariant as it does not vary voltage and current magnitudes.

Differentiating the expression of \bar{v}_h in (5) gives:

$$\begin{aligned} \dot{\bar{v}}'_h &= -j\dot{\delta} \exp(-j\delta) \bar{v}_h + \exp(-j\delta) \bar{\eta}_v \bar{v}_h, \\ &= (\bar{\eta}_v - j\dot{\delta}) \bar{v}'_h. \end{aligned} \quad (6)$$

Hence, the CF of a voltage referred to a local rotating reference frame is:

$$\bar{\eta}'_v = \bar{\eta}_v - j\dot{\delta}. \quad (7)$$

A similar expression can be obtained for the current:

$$\bar{\eta}'_i = \bar{\eta}_i - j\dot{\delta}. \quad (8)$$

In the remainder of the paper, the operators $\bar{\eta}$ and $\bar{\eta}'$ are utilized to indicate the time derivative of relevant time-dependent complex quantities (e.g., the state variables and reference currents of the converter controllers) on grid and local reference frames, respectively.

III. GENERAL DERIVATIONS AND CURRENT CONTROL

Using Park vectors, the instantaneous power injected at a bus h can be written as a complex quantity, as follows:

$$\bar{s}_h = \bar{v}_h \bar{i}_h^*, \quad (9)$$

where $*$ denotes the complex conjugate operator. The time derivative (rate of change) of complex power is:

$$\begin{aligned} \dot{\bar{s}}_h &= \dot{\bar{v}}_h \bar{i}_h^* + \bar{v}_h \dot{\bar{i}}_h^* \\ &= \bar{\eta}_v \bar{v}_h \bar{i}_h^* + \bar{v}_h \bar{\eta}_i^* \bar{i}_h^* \\ &= (\bar{\eta}_v + \bar{\eta}_i^*) \bar{s}_h. \end{aligned} \quad (10)$$

Using (7) and (8), (10) can be rewritten using the complex frequencies on the device local reference frame:

$$\begin{aligned} \dot{\bar{s}}_h &= [\bar{\eta}_v + j\dot{\delta} - j\dot{\delta} + \bar{\eta}_i^*] \bar{s}_h \\ &= [\bar{\eta}'_v + (\bar{\eta}'_i)^*] \bar{s}_h. \end{aligned} \quad (11)$$

Expression (10) is general for any device connected to the grid while expression (11) is general for any device that has a synchronization mechanism that aligns the dq reference frame of the device with that of the grid.

A. Ideal controllers

The most common ideal models of devices connected to the grid are considered in this section as they represent the

operation of ideal (i.e., perfect tracking and infinitely fast) generators and converter controllers. In the continuation, (10) is coupled with the characteristics of each device. This allows to determine the impact of these ideal devices on the CF of the voltage and the current.

1) *Ideal Voltage Source (Slack Bus)*: An ideal slack bus has:

$$\dot{\bar{v}}_h = 0, \quad \bar{\eta}_v = 0, \quad (12)$$

From (12), (10) becomes:

$$\dot{\bar{s}}_h = \bar{\eta}_i^* \bar{s}_h, \quad (13)$$

which indicates that an ideal slack bus affects only the frequency of the injected current, but not the voltage.

2) *Ideal Current Source*: An ideal current source that can impose both the magnitude and the phase of the current:

$$\dot{\bar{i}}_h = 0, \quad \bar{\eta}_i = 0, \quad (14)$$

leading to:

$$\dot{\bar{s}}_h = \bar{\eta}_v \bar{s}_h. \quad (15)$$

3) *Current Source with Constant Power Factor*: More commonly, an ideal current source imposes the magnitude and a constant power factor [18]. This results in:

$$\rho_i = 0, \quad \omega_v = \omega_i, \quad (16)$$

and thus:

$$\dot{\bar{s}}_h = \rho_v \bar{s}_h. \quad (17)$$

4) *Constant Power*: For an ideal constant power load or source:

$$\dot{\bar{s}}_h = 0, \quad \bar{\eta}_v = -\bar{\eta}_i^*, \quad (18)$$

which indicates that the complex frequencies of both voltage and current change, but not independently.

5) *Constant Admittance*: For an ideal admittance, the magnitude of current is proportional to the one of the voltage while their phases vary only by the constant angle of the admittance. This directly dictates that [18]:

$$\rho_v = \rho_i, \quad \omega_v = \omega_i, \quad (19)$$

and from (10):

$$\dot{\bar{s}}_h = 2\rho_v \bar{s}_h. \quad (20)$$

This is consistent with the fact that an admittance cannot affect the frequency at a bus. Equations (17) and (20) reveal that an ideal admittance and an ideal current source with constant power factor have a similar dynamic response.

6) *PV Generator*: Lastly, an ideal PV generator has constant voltage magnitude and constant active power:

$$\rho_v = 0, \quad \dot{p} = 0. \quad (21)$$

Combining the two and substituting in (10) leads to:

$$\frac{q}{p} = \frac{\rho_i}{(\omega_v - \omega_i)}. \quad (22)$$

where p and q are the active and reactive power components of \bar{s}_h , respectively. Equation (22) leads to the non-intuitive conclusion that the reactive power at a PV bus can be changed

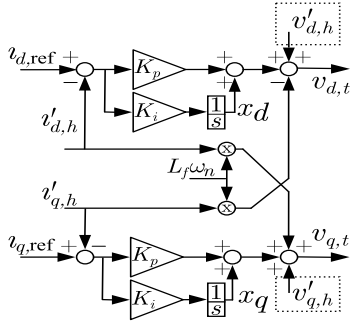


Fig. 1. Control diagram of a PI-based current control in the synchronous reference frame. Optional VFF are specifically marked with dotted boxes.

not only by varying the voltage magnitude but also by varying either the frequency of the voltage and/or of the current.

B. Current Controller

Due to practical considerations (e.g., over-current limiting and resonance damping) an inner current controller is ubiquitous in VSC applications [4]. Figure 1 shows a control diagram of such a controller. The dynamic equation of a current flowing through the output inductor L of a converter is:

$$\bar{v}_t - \bar{v}_h = L_f \dot{\bar{i}}_h + R_f \bar{i}_h, \quad (23)$$

where L_f is the filter inductance, R_f its parasitic resistance and $\bar{v}_t = v_{d,t} + jv_{q,t}$ is the modulated voltage output of the converter. From Figure 1, the control equations can be derived as:

$$\begin{aligned} \bar{v}_t &= \bar{v}_h' + j\omega_n L_f \bar{i}_h' + K_p(\bar{i}_{\text{ref}} - \bar{i}_h') + K_i \bar{x}, \\ \dot{\bar{x}} &= \bar{i}_{\text{ref}} - \bar{i}_h' \end{aligned} \quad (24)$$

where K_p, K_i are the proportional and integral gains of the PI controller, respectively, $\bar{x} = x_d + jx_q$ is the complex internal state of the integral part of the controller and $\bar{i}_{\text{ref}} = i_{d,\text{ref}} + j i_{q,\text{ref}}$ is the current reference signal. By neglecting the synchronization mismatches ($\bar{v}_h' \approx \bar{v}_h$, $\bar{i}_h' \approx \bar{i}_h$), the electromagnetic dynamics of the L -filter ($L_f \dot{\bar{i}}_h = L_f \bar{\eta}_h \bar{i}_h \approx \omega_n L_f \bar{i}_h$) and its resistance ($R_f \approx 0$), and by substituting equation (24) to (23), one derives [28]:

$$\begin{aligned} 0 &= K_p(\bar{i}_{\text{ref}} - \bar{i}_h') + K_i \bar{x}, \\ \dot{\bar{x}} &= \bar{i}_{\text{ref}} - \bar{i}_h'. \end{aligned} \quad (25)$$

Differentiating the algebraic equation in (25), one has:

$$\begin{aligned} \bar{\eta}_h' \bar{i}_h' &= \dot{\bar{i}}_{\text{ref}} + \kappa_{\text{PI}} \dot{\bar{x}} \\ &= \bar{\eta}_{i_{\text{ref}}} \bar{i}_{\text{ref}} + \kappa_{\text{PI}} (\bar{i}_{\text{ref}} - \bar{i}_h') \\ &= (\bar{\eta}_{i_{\text{ref}}} + \kappa_{\text{PI}}) \bar{i}_{\text{ref}} - \kappa_{\text{PI}} \bar{i}_h'. \end{aligned} \quad (26)$$

where $\kappa_{\text{PI}} = K_i/K_p$. Equation (26) can be also written as:

$$(\bar{\eta}_h' + \kappa_{\text{PI}}) \bar{i}_h' = (\bar{\eta}_{i_{\text{ref}}} + \kappa_{\text{PI}}) \bar{i}_{\text{ref}}, \quad (27)$$

which shows that the coefficient κ_{PI} , and hence the PI controller effect, can be interpreted as a constant real translation that affects only the magnitude. Then, substituting (26) into (11) leads to:

$$\dot{\bar{s}}_h = (\bar{\eta}_{i_{\text{ref}}}^* + \kappa_{\text{PI}}) \bar{v}_h' \bar{i}_{\text{ref}}^* + (\bar{\eta}_v' - \kappa_{\text{PI}}) \bar{s}_h. \quad (28)$$

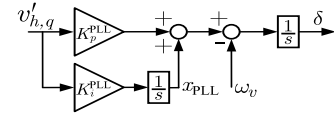


Fig. 2. Control diagram of synchronous reference frame PLL.

Equation (28) separates the effect of the inner current control from the synchronization mechanism and the outer control loops. Moreover, if the dynamic of the PI can be assumed fast, $\bar{i}_{\text{ref}} \approx \bar{i}_h'$ and hence $\bar{\eta}_{i_{\text{ref}}} \approx \bar{\eta}_h'$. Then (28) simplifies to (11). Finally we note that the coefficients of \bar{i}' and \bar{v}' that appears in (27) and (28), respectively, can be written as:

$$\begin{aligned} (\bar{\eta}_h')^* + \kappa_{\text{PI}} &= \bar{\eta}_h^* + (\kappa_{\text{PI}} + j\dot{\delta}), \\ \bar{\eta}_v' - \kappa_{\text{PI}} &= \bar{\eta}_v - (\kappa_{\text{PI}} + j\dot{\delta}). \end{aligned} \quad (29)$$

The complex quantity $\kappa_{\text{PI}} + j\dot{\delta}$ has the dimension of a complex frequency and embeds the effects of the synchronization mechanism and of the current control. The equation is general and can be applied to both synchronous machines and controllers with an internal current loop. For a synchronous machine $\kappa_{\text{PI}} = 0$, whereas for an ideal synchronization (e.g., ideal PLL), $j\dot{\delta} \approx 0$ because $\delta \approx 0$. The utilization of the CF allows thus to easily identify and separate the dynamic effects and non-ideality of the controllers of conventional and converter-interfaced devices connected to the grid.

C. Voltage Feed-Forward (VFF)

Equation (25) assumes that a VFF is included in the current controller [28]. If the VFF is not included, (25) becomes:

$$\bar{i}_h' = \bar{i}_{\text{ref}} + \frac{1}{K_p} (K_i \bar{x} - \bar{v}_h'), \quad (30)$$

which leads to:

$$(\bar{\eta}_h' + \kappa_{\text{PI}}) \bar{i}_h' = (\bar{\eta}_{i_{\text{ref}}} + \kappa_{\text{PI}}) \bar{i}_{\text{ref}} - \frac{1}{K_p} \bar{\eta}_v' \bar{v}_h', \quad (31)$$

and, finally:

$$\dot{\bar{s}}_h = (\bar{\eta}_{i_{\text{ref}}}^* + \kappa_{\text{PI}}) \bar{v}_h' \bar{i}_{\text{ref}}^* + (\bar{\eta}_v' - \kappa_{\text{PI}}) \bar{s}_h - \frac{1}{K_p} (\bar{\eta}_v')^* v_h'^2, \quad (32)$$

where $v_h = v_h'$ is the magnitude of \bar{v}_h' . This result indicates that the dynamic effect of the VFF is inversely proportional to K_p and that it modulates the CF of voltage \bar{v}_h .

IV. GFL CONVERTERS

GFL converters typically measure or estimate the frequency and phase of the voltage at the converter connection point and then use these measurements to synchronize with the grid [4]. Typically, this measurement is achieved through a PLL device. A common PLL synchronization strategy is to set the voltage q component equal to zero by using a PI controller. In that case, the output of the PLL provides the angle that is used for the transformation between converter-side and grid-side variables. A control diagram of a common PLL is shown in Fig. 2. The synchronization strategy is given by [29]:

$$\begin{aligned} \dot{x}_{\text{PLL}} &= \Im\{\bar{v}_h'\}, \\ \dot{\delta} &= K_p^{\text{PLL}} \Im\{\bar{v}_h'\} + K_i^{\text{PLL}} x_{\text{PLL}} - \omega_v, \end{aligned} \quad (33)$$

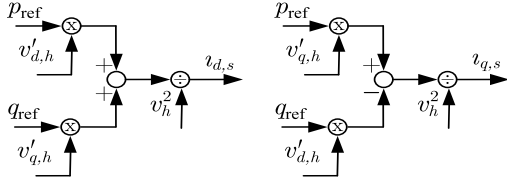


Fig. 3. Block diagram for the calculation of current reference from active and reactive power commands.

where K_p^{PLL} , K_i^{PLL} are the proportional and integral gains of the PI controller included in the PLL, \Im is the imaginary part operator and ω_v is the frequency at the connection bus. Many other PLL implementations are reported in the literature [29, 30]. Equation (33) can be substituted back into equations (7) and (8) so that the effect of the PLL parameters to the CF can be directly evaluated.

In the following subsections, expressions for the terms \bar{i}_{ref} and $\bar{\eta}_{i_{\text{ref}}}$ (or $\bar{\eta}_{i_{\text{ref}}} \bar{i}_{\text{ref}}$) are provided for relevant GFL control configurations that are typically found in practical applications. Then, these expressions are coupled with (28) and (33) to derive the expression of $\dot{\bar{s}}_h$.

A. Current controller with constant current reference

In this simplified case, the current controller tracks a constant current reference. Thus, the expressions for \bar{i}_{ref} and $\bar{\eta}_{i_{\text{ref}}}$ are immediately deduced as:

$$\begin{aligned} \bar{i}_{\text{ref}} &= \text{const.}, \\ \Rightarrow \bar{\eta}_{i_{\text{ref}}} &= 0, \end{aligned} \quad (34)$$

and substituting into (28):

$$\dot{\bar{s}}_h = \kappa_{\text{PI}} \bar{v}_h' \bar{i}_{\text{ref}}^* + (\bar{\eta}_v' - \kappa_{\text{PI}}) \bar{s}_h. \quad (35)$$

For an ideal current source, $\bar{i}_{\text{ref}} = \bar{i}$ and substituting $\bar{v}_h' \bar{i}_{\text{ref}}^* = \bar{s}_h$, (35) simplifies to (15). With the use of (25), equation (35) can be re-written in terms of the controller internal states as:

$$\dot{\bar{s}}_h = \bar{s}_h \bar{\eta}_v - \kappa_{\text{PI}} \bar{x}^* \bar{v}_h' = \bar{s}_h \bar{\eta}_v + \Delta \bar{s}_h. \quad (36)$$

In the following, (36) is utilized to highlight the effect of the non-ideal current controller in comparison with the ideal current source of (15).

B. Current Controller with Constant Power Reference

In practical applications, a constant power reference (\bar{s}_{ref}) is often preferred over a current reference [31]. Then:

$$\begin{aligned} \bar{i}_{\text{ref}} &= \bar{i}_s = \left(\frac{\bar{s}_{\text{ref}}}{\bar{v}_h'} \right)^*, \\ \Rightarrow \bar{\eta}_{i_{\text{ref}}} \bar{i}_{\text{ref}} &= \left(-\frac{\bar{s}_{\text{ref}}}{\bar{v}_h'} \bar{\eta}_v' \right)^* \\ &= -\bar{i}_{\text{ref}} (\bar{\eta}_v')^*, \\ \Rightarrow \bar{\eta}_{i_{\text{ref}}} &= -(\bar{\eta}_v')^*, \end{aligned} \quad (37)$$

leading to:

$$\dot{\bar{s}}_h = (\bar{\eta}_v' - \kappa_{\text{PI}}) (\bar{s}_h - \bar{s}_{\text{ref}}). \quad (38)$$

For an ideal PQ source $\bar{s}_h = \bar{s}_{\text{ref}}$, which leads to simplify (38) to (18). A block diagram for the calculation of the current

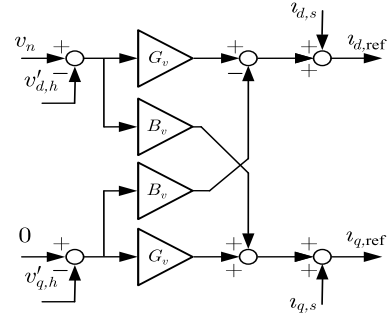


Fig. 4. Control diagram of a virtual admittance loop.

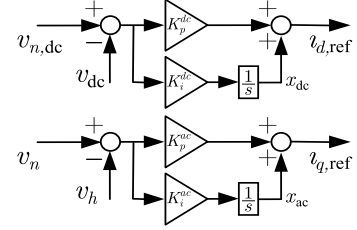


Fig. 5. Control diagram of the outer loops for GFL applications.

reference from the active and reactive power commands is shown in Fig. 3.

C. Current Controller with Virtual Admittance Loop

Reference [32] proposes a virtual admittance control loop able to provide voltage support in resistive or weak grids. A control diagram of this loop can be seen in Fig. 4. This loop emulates the operation of an admittance $\bar{Y}_v = G_v + jB_v$ in order to follow a voltage reference $\bar{v}_{\text{ref}} = v_n + j0$, where v_n is the nominal voltage ($\bar{v}_{\text{ref}} = \bar{v}_{\text{ref}}^*$). In the literature, converters that provide ancillary services to the grid are also referred to as grid-supporting converters [5]. However, since these controllers utilizes identical PLL and current controllers, they can be included in the GFL category for ease of reference. The equations are:

$$\begin{aligned} \bar{i}_{\text{ref}} &= \bar{i}_s + \bar{Y}_v (\bar{v}_{\text{ref}} - \bar{v}_h') \\ &= \left(\frac{\bar{s}_{\text{ref}}}{\bar{v}_h'} \right)^* + \bar{Y}_v (\bar{v}_{\text{ref}} - \bar{v}_h'), \\ \Rightarrow \bar{\eta}_{i_{\text{ref}}} \bar{i}_{\text{ref}} &= \left(-\frac{\bar{s}_{\text{ref}}}{\bar{v}_h'} \bar{\eta}_v' \right)^* - \bar{Y}_v \bar{v}_h' \bar{\eta}_v', \end{aligned} \quad (39)$$

where \bar{i}_s denotes the current calculated by the power reference as in the previous case. By substituting:

$$\begin{aligned} \dot{\bar{s}}_h &= (\bar{\eta}_v' - \kappa_{\text{PI}}) (\bar{s}_h - \bar{s}_{\text{ref}}) \\ &\quad + \bar{Y}_v^* (-v_h^2 ((\bar{\eta}_v')^* + \kappa_{\text{PI}}) + \kappa_{\text{PI}} \bar{v}_h' \bar{v}_{\text{ref}}). \end{aligned} \quad (40)$$

Assuming ideal current control ($\kappa_{\text{PI}} = 0$), (40) simplifies to:

$$\dot{\bar{s}}_h = -v_h^2 \bar{Y}_v^* 2\rho_v + \bar{Y}_v^* \bar{\eta}_v' \bar{v}_h' \bar{v}_{\text{ref}}. \quad (41)$$

The first term corresponds to the power consumed by the virtual admittance and is consistent with (20), whereas the second term corresponds to the voltage reference.

D. Current Controller with Outer Control Loops

GFL converters can be used for applications different than power delivery from distributed sources [31]. Most notable is the case of GFL rectifiers that are tasked with maintaining dc-link voltage v_{dc} equal to its nominal value $v_{n,dc}$ of an electronically-interfaced load [33]. This is achieved through an outer-loop that calculates the d -axis current reference [28, 34]. Therefore, the q -axis current is free to provide voltage support. This is usually achieved through an outer droop controller but a PI regulator can also be used [35, 36]. In this study, a PI is used for generality. A control diagram of these outer loops can be seen in Fig. 5.

The current references are calculated as:

$$\begin{aligned} i_{d,ref} &= K_p^{dc}(v_{n,dc} - v_{dc}) + K_i^{dc}x_{dc}, \\ i_{q,ref} &= K_p^{ac}(v_n - v_h) + K_i^{ac}x_{ac}, \end{aligned} \quad (42)$$

where K_p^{dc} , K_i^{dc} are the proportional and integral gains, respectively, of the outer dc voltage PI controller, K_p^{ac} , K_i^{ac} are the proportional and integral gains, respectively, of the outer ac voltage PI controller, v_n is the nominal voltage rate of the connection bus, and the internal PI states are:

$$\begin{aligned} \dot{x}_{dc} &= v_{n,dc} - v_{dc}, \\ \dot{x}_{ac} &= v_n - v_h. \end{aligned} \quad (43)$$

By using the definition of the real part of the CF (3), equation (42) and its derivative can be written using complex notation as:

$$\begin{aligned} \bar{i}_{ref} &= K_p^o(\bar{v}_{ref}^o - \bar{v}_o) + K_i^o\bar{x}_o, \\ \Rightarrow \bar{\eta}_{i,ref}\bar{i}_{ref} &= -\bar{v}_o(K_p^o\bar{\rho} + K_i^o) + K_i^o\bar{v}_{ref}^o, \end{aligned} \quad (44)$$

where $K_p^o = K_p^{dc} = K_p^{ac}$, $K_i^o = K_i^{dc} = K_i^{ac}$, $\bar{x}_o = x_{dc} + jx_{ac}$, $\bar{v}_{ref}^o = v_{n,dc} + jv_n$, $\bar{v}_o = v_{dc} + v_h$ and $\bar{\rho} = \rho_{dc} + j\rho_v$. The assumption of equal controller gains for the two dq -axes is consistent if a proper pu base for the dc voltage is selected so that $v_{n,dc} = v_n$. This is straightforward as the dc voltage is independent from the rest of the system and typically ac and dc voltages are selected in the same order of magnitude [28]. Equation (44) indicates that the outer control loops only affect quantity $\bar{\rho}$ (i.e., the magnitude of ac and dc voltage) but not frequency ω_v .

V. GFM CONVERTERS

In this section, the analytical expressions for \bar{i}_{ref} , $\bar{\eta}_{i,ref}\bar{i}_{ref}$ and \dot{s} are derived, considering the inner voltage controllers for GFM control configurations. Then, different power-based synchronization and voltage regulation strategies that are commonly found in the literature are presented.

A. Voltage Controller

A set of equations that describes a PI-based, voltage controller is the following:

$$\begin{aligned} \dot{\bar{x}}_v &= \bar{v}_{ref} - \bar{v}_h', \\ \bar{i}_{ref} &= K_p^v(\bar{v}_{ref} - \bar{v}_h') + K_i^v\bar{x}_v, \\ \bar{\eta}_{i,ref}\bar{i}_{ref} &= (K_p^v\bar{\eta}_{v,ref}' + K_i^v)\bar{v}_{ref} - (K_p^v\bar{\eta}_v' + K_i^v)\bar{v}_h'. \end{aligned} \quad (45)$$

where \bar{v}_{ref} is the voltage reference from an outer loop, e.g., a voltage droop controller. The control diagram of the outer

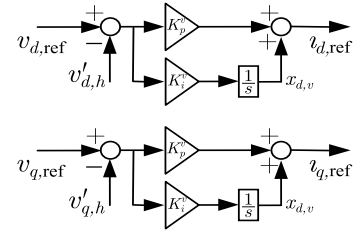


Fig. 6. Control diagram of a PI-based voltage controller used in GFM applications.

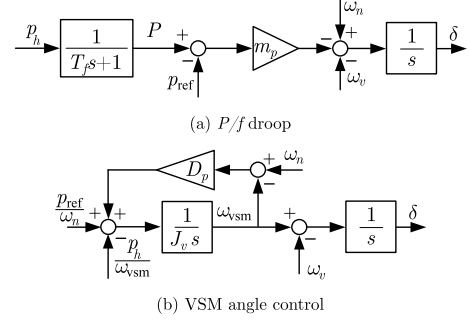


Fig. 7. Control diagram of the active power synchronization strategies. (a) P/f droop and (b) VSM angle control.

voltage controller for GFM applications is shown in Fig. 6. To decouple the effects of the voltage and the current controllers, it is assumed that $\bar{\eta}_{i,ref}^* + \kappa_{PI} \approx \bar{\eta}_{i,ref}^*$. Thus, by substituting the third equation of (45) into (28), one has:

$$\begin{aligned} \dot{s}_h &= (K_p^v\bar{\eta}_{v,ref}' + K_i^v)\bar{v}_h'\bar{v}_{ref}^* \\ &\quad - (K_p^v(\bar{\eta}_v')^* + K_i^v)v_h^2 + (\bar{\eta}_v' - \kappa_{PI})\bar{s}_h. \end{aligned} \quad (46)$$

The above equation indicates that gain K_p^v modulates the frequency of the voltage in a similar way as gain K_p^o modulates the quantity $\bar{\rho}$ in (44).

B. Power-Based Synchronization Strategies

This section discusses the expressions for \dot{s} based on the widely known active power-frequency droop (P/f droop) and VSM concepts. Control diagrams for these two synchronization strategies can be seen in Fig. 7. Various other implementations for the outer frequency/phase controllers have been proposed and the optimal controller selection for different scenarios is still an open research topic [3].

The equations for the P/f droop are the following [9, 10]:

$$\begin{aligned} \dot{\delta} &= \omega_n - \omega_v - m_p(P - p_{ref}), \\ T_f \dot{P} &= p_h - P, \end{aligned} \quad (47)$$

where m_p is the droop gain and T_f is the time constant of the (optional) low-pass filter. Lowercase p_h is the active power injection and uppercase P is the filtered active power. For the VSM, a common implementation in the literature is the following [11–13]:

$$\begin{aligned} \dot{\delta} &= \omega_{VSM} - \omega_v, \\ \dot{\omega}_{VSM} &= \frac{1}{J_v} \left(\frac{p_{ref}}{\omega_n} - \frac{p_h}{\omega_{VSM}} + D_p(\omega_n - \omega_{VSM}) \right), \end{aligned} \quad (48)$$

where J_v is the moment of virtual inertia coefficient while D_p is the virtual damping coefficient. It should be noted that

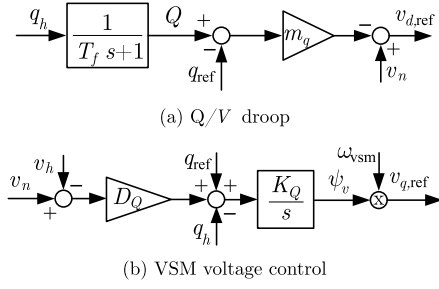


Fig. 8. Control diagram of the outer voltage loops for GFM applications. (a) Q/V droop and (b) VSM voltage control.

moment of inertia J is a distinct quantity than the mechanical starting time M and only coincide when pu values are being used.

C. Outer Voltage Loop

This section discusses the outer voltage loop that defines the quantity $\bar{v}_{\text{ref}} = v_{d,\text{ref}} + jv_{q,\text{ref}}$. By obtaining the analytical expressions for \bar{v}_{ref} and $\dot{\bar{v}}_{\text{ref}}$, they can be substituted into (46). Typically, reactive power/voltage (Q/V) droop controllers, PI/integral-based controllers or a combination of the two are preferred [3]. The control diagrams for the voltage regulation loops for the Q/V droop strategy and the VSM voltage control strategy are shown in Fig. 8.

For the droop controller, the voltage is aligned with the d -axis of the voltage. That results in:

$$\begin{aligned} \bar{v}_{\text{ref}} &= v_{d,\text{ref}} = v_n - m_q(Q - q_{\text{ref}}), \\ T_f \dot{Q} &= q_h - Q, \end{aligned} \quad (49)$$

where lowercase q is the reactive power injection and uppercase Q is the filtered reactive power. Differentiating one gets:

$$\bar{\eta}_{v,\text{ref}} \bar{v}_{\text{ref}} = \dot{v}_{d,\text{ref}} = \frac{m_q}{T_f}(Q - q_h). \quad (50)$$

By observing that $\bar{v}_{\text{ref}} = v_{d,\text{ref}}$ leads directly to $\bar{\eta}_{v,\text{ref}} \bar{v}_{\text{ref}} = (\bar{\eta}_{v,\text{ref}} \bar{v}_{\text{ref}})^*$, one can simplify (50) to:

$$\bar{\eta}_{v,\text{ref}} \bar{v}_{\text{ref}} = \rho_{v,\text{ref}} v_{d,\text{ref}} = \frac{m_q}{T_f}(Q - q_h). \quad (51)$$

An example of a combination of integral and droop controller for the voltage regulation can be found in [13]. This strategy is paired with the VSM synchronization control of equation (48). In it, the equivalence with physical quantities is preserved by defining the virtual flux as:

$$\dot{\psi}_v = K_Q(q_{\text{ref}} - q_h + D_Q(v_n - v_h)), \quad (52)$$

where K_Q is the integral gain and D_Q is the droop gain. The output of the outer voltage controller is then aligned with the q -axis of the voltage as in:

$$\begin{aligned} \bar{v}_{\text{ref}} &= jv_{q,\text{ref}} = j\psi_v \omega_{\text{VSM}}, \\ \Rightarrow \bar{\eta}_{v,\text{ref}} \bar{v}_{\text{ref}} &= j(\dot{\psi}_v \omega_{\text{VSM}} + \psi_v \dot{\omega}_{\text{VSM}}), \end{aligned} \quad (53)$$

where $\dot{\psi}_v$ is given by (52) and $\dot{\omega}_{\text{VSM}}$ is given by (48). Similar to the previous case, one observes that again $\bar{\eta}_{v,\text{ref}} = \rho_{v,\text{ref}}$. It can be concluded then that when either the real or the imaginary part of the outer loop reference is set to zero, the outer loop

TABLE I
SUMMARY OF THE INTERNAL FREQUENCY EXPRESSIONS

Control Configuration	Internal Frequency	Equations
Current control + PLL	$\bar{\eta}_v - j\dot{\delta} - \kappa_{\text{PI}}$	(7), (33), (35), (38)
Effect of VFF	$-\frac{1}{K_p}(\bar{\eta}_v^* + j\dot{\delta})$	(7), (32), (33)
Virtual admittance	$-v_h^2 \bar{Y}_v^* ((\bar{\eta}_v')^* + \kappa_{\text{PI}})$	(7), (33), (40)
GFL outer loops	$K_p^o \bar{\rho} + K_i^o$	(44)
GFM voltage control	$-(K_p^v (\bar{\eta}_v')^* + K_i^v)$	(46)
P/f droop control	$\bar{\eta}_v - j\dot{\delta}$	(7), (47)
VSM angle control	$\bar{\eta}_v - j\dot{\delta}$	(7), (48)

does not modify the frequency of the reference signal, only its magnitude. This is consistent with the original design of the outer voltage loops.

For ease of reference, all the internal frequencies derived in Sections IV and V are summarized in Table I. Once these internal frequencies are defined, one can compare the dynamic performance of converter control based on the bus frequency and on the *internal* ones, and also understand how the parameters of the these controllers affect the internal frequency and, then, again, the control itself. This study is particularly relevant in the case of electronic converters as their controllers can be fast and thus even relatively small differences in the value of the measured frequency can lead to visible differences in their dynamic performance.

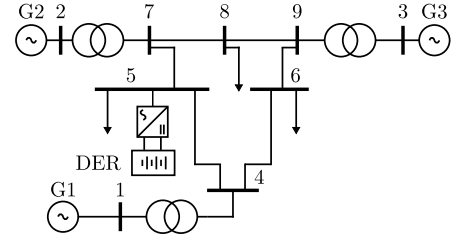


Fig. 9. Single-line diagram of the modified WSCC 9-bus system.

VI. SIMULATION RESULTS

To illustrate the theoretical developments, different case studies considering the WSCC 9-bus system are presented in this section. The purpose of the case study is to show how the CF can be used as a *metric* for the dynamic performance of the synchronization mechanisms and controllers of grid-connected converters. The synchronous generators are modeled using conventional 4th order models. A converter-interfaced energy storage system is connected to bus 5 of the grid through an LC -filter, modeled as in [37]. Although its dynamic effects has been neglected in the analytical developments above, the ac filter is included in the models utilized in the simulations. A schematic of the network that was used for all simulations is shown in Figure 9. The CF components ρ_v and ω_v are calculated using the procedure described in [18]. All simulations were carried out with the Dome software tool [38]. For the examples regarding the effect of the PLL and the current control, a standard SRF-PLL described by (33) is used. The current references are kept constant and tracked by a PI controller as in (25). The dc voltage is kept constant

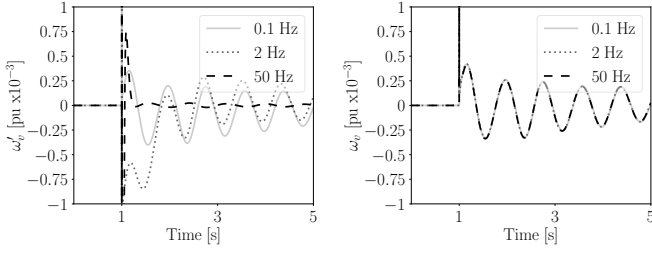


Fig. 10. Frequency deviation referred to the converter reference frame and as seen at bus 5 of the WSCC 9-bus system during the disconnection at $t = 1$ s of the load at bus 5. PLL gains are set for various controller bandwidth values.

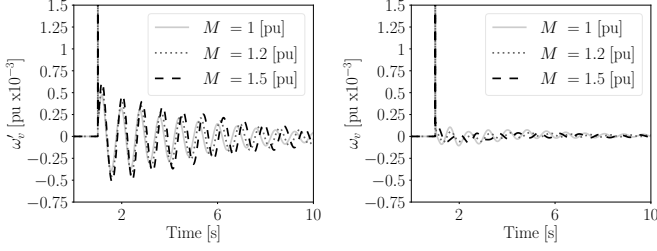


Fig. 11. Frequency deviation referred to the synchronous machine rotor and as seen at bus 1 of the WSCC 9-bus system during the disconnection at $t = 1$ s of the load at bus 5. The simulation is repeated for different values of M .

by an ideal voltage source. For the example on the outer controllers, the ideal voltage source is swapped for a capacitor of $C_{dc} = 0.05$ F and the outer loops of (42) and (43) are used. Lastly, for the GFM configurations, the outer voltage loop of (45) are used to regulate the voltage. Equations (47) and (49) are used to define the droop-based, GFM control while (48), (52) and (53) are used for the VSM control. In the latter case, an ideal voltage source is again used to regulate the dc voltage. The contingency that is used for all examples is a disconnection of the load at bus 5 at $t = 1$ s. If not explicitly stated otherwise, all frequency-like quantities in this section refer to frequency deviations from the nominal values ($\rho_v = 0$ and $\omega_v = 1$ pu).

A. Effect of the PLL

Fig. 10 shows the imaginary part of the CF ω'_v referred to the converter reference frame (equation (7)) as well as the frequency ω_v , as seen at the converter bus. The PLL gains are tuned so that the PLL damping is always one while its bandwidth varied. While the frequency at the bus is unaffected by the PLL gains, the frequency referred to the converter is dictated by the PLL dynamics. A parallel for PLL case can be drawn with the case of the synchronous machine. For that device, “internal” frequency ω'_v can be calculated with equation (7) where in that case, δ is the rotor speed referred to the frequency at the center of inertia, namely $\dot{\delta} = \omega_r - \omega_{COI}$. Fig. 11 shows the frequency deviation referred to the synchronous machine rotor and at bus 1 after the contingency for different values of the mechanical starting time M . The mechanical starting time is defined as $M = 2H$, where H is the inertia constant of a synchronous machine [39]. The two quantities are often used interchangeably in the literature to describe the inertia properties of a synchronous machine [39, 40]. The parameter change affects both quantities, but it can be seen

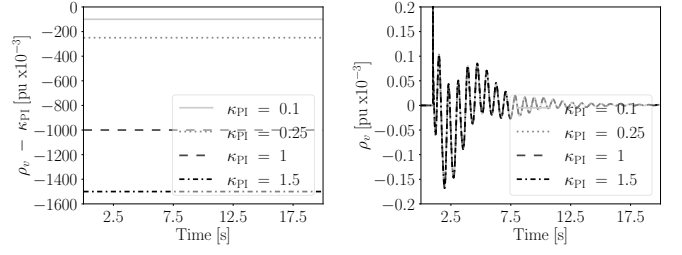


Fig. 12. Real part of the CF ρ_v , translated by the effect of the PI current controller and as seen at bus 5 during the contingency for different values of κ_{PI} .

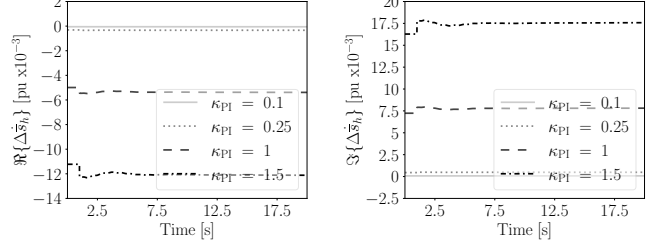


Fig. 13. Real and imaginary part of the quantity $\Delta\tilde{s}_h$, quantifying the non-ideality of the current control. Simulation for disconnection at $t = 1$ s of the load at bus 5 and different values of κ_{PI} .

that the internal frequency undergoes larger variations. The above examples illustrates that while the internal frequency for the synchronous machine is well defined and understood, this is not the case for the different converter controllers. The proposed method helps to overcome this problem by clearly defining it for the different synchronization methods. It is shown in Section VI-G how this method can be used for control applications.

B. Non-Ideality of the Current Controller

Fig. 12 shows the translation in the CF caused by the internal current PI as well as the real part of the CF at the converter bus. It can be seen that the variation of ρ_v is negligible compared to the constant translation caused by the PI. A better way to illustrate the non-ideality of the current controller is by plotting its deviation from an ideal current controller $\Delta\tilde{s}_h$, calculated with (36). Fig. 13 shows the real and imaginary parts of this quantity for different values of parameter κ_{PI} . For larger values of the parameter, the operation of the controller increasingly deviates from the ideal case, namely $\kappa_{PI} = 0$.

C. Effect of the VFF

Figs. 14 and 15 show the real and imaginary part of the CF at bus 5 for different values of current control proportional gain K_p . The simulation is repeated with the VFF being switched on and off for each value of the controller gain. If the VFF is active, the change of the parameter does not affect neither of the two components of the CF. If the VFF is switched off, the gain modulates the frequency, as predicted by (32).

D. Effect of the Outer Loops

Fig. 16 shows the effect on the CF of the variation of gain K_p^o of the outer control loops in the GFL control of (44).

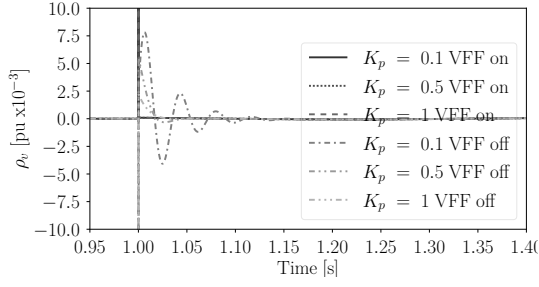


Fig. 14. Real part of the CF as seen at bus 5 of the WSCC 9-bus system during the disconnection at $t = 1$ s of the load at bus 5. Simulation for different values of parameter K_p and VFF enabled and disabled.

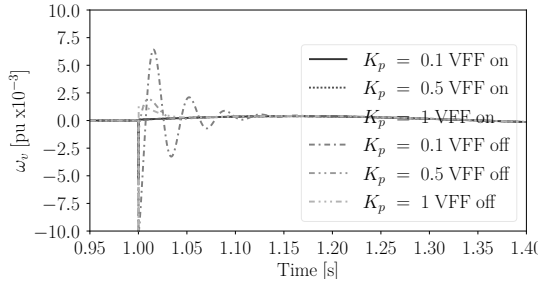


Fig. 15. Imaginary part of the CF as seen at bus 5 of the WSCC 9-bus system during the disconnection at $t = 1$ s of the load at bus 5. Simulation for different values of parameter K_p and VFF on and off.

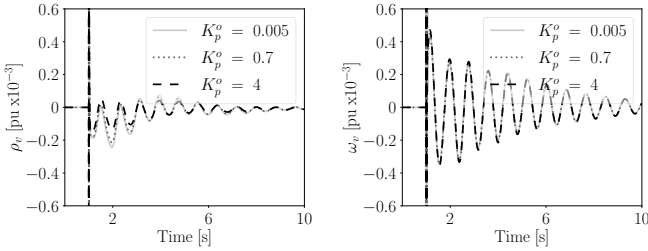


Fig. 16. Real and imaginary part of the CF as seen at bus 5 of the WSCC 9-bus system during the disconnection at $t = 1$ s of the load at bus 5. Simulation for different values of parameter K_p^o of the outer voltage loops in the GFL control configuration.

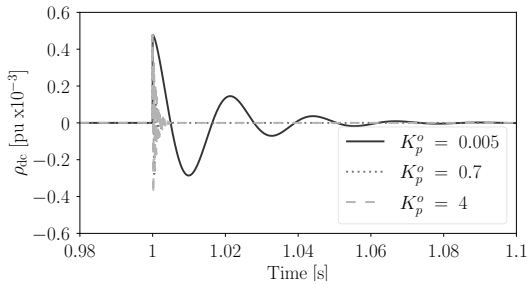


Fig. 17. dc "frequency" during the contingency at $t = 1$ s. Simulation for different values of parameter K_p^o of the outer voltage loops in the GFL control configuration.

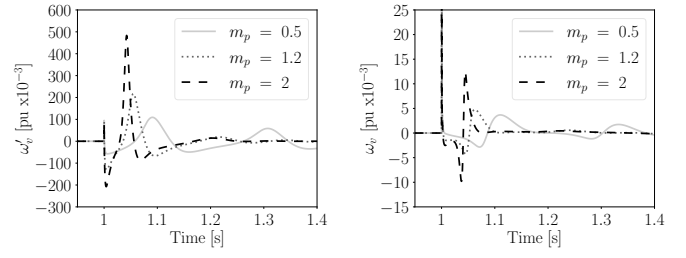


Fig. 18. Frequency deviation referred to the converter reference frame and as seen at bus 5 of the WSCC 9-bus system during the disconnection at $t = 1$ s of the load at bus 5. The simulation is repeated for different values of the active power droop parameter m_p .

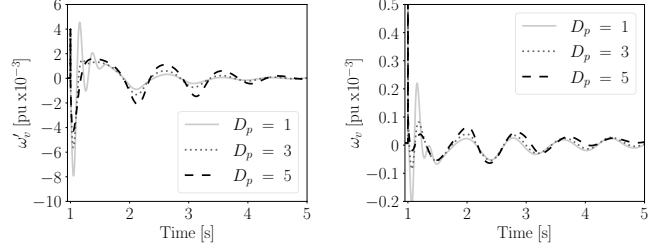


Fig. 19. Frequency deviation referred to the converter reference frame and as seen at bus 5 of the WSCC 9-bus system during the disconnection at $t = 1$ s of the load at bus 6. The simulation is repeated for different values of the VSM damping parameter D_p .

Results confirm that only ρ_v is affected while ω_v remains identical. Fig. 17 shows the variation of ρ_{dc} for the same set of parameters. For this specific dc-side topology, ρ_{dc} is calculated by standard circuit variables available from the software ($\rho_{dc} = \dot{v}_{dc}/v_{dc} = i_{dc}/(C_{dc}v_{dc})$). Although the transient effect diminishes quickly for higher gain values, it can be seen that changing gain K_p^o has the expected effect on the quantity ρ_{dc} . The modulation of both ρ_v , ρ_{dc} by parameter K_p^o justifies the use of the generalized quantity $\bar{\rho}$ in (44). The use of identical gains for the dq channels, without loss of stability, also justifies the complex notation of (44). For this specific application, the ratio of dc to ac voltage is: $v_{n,dc}/v_n = 0.35$.

E. Effect of the Active Power Droop

Fig. 18 shows the effect of the active power droop parameter m_p on the internal frequency and on the frequency at the converter bus after the contingency. The effect of this outer-loop parameter on the frequency is more impactful than the previous cases that concern controllers with faster time scales. Particularly for the internal frequency, the time response is separated by a full order of magnitude compared to the frequency at the bus. Finally, note that although the effects are larger for this case, the selected unit for the figures ($\text{pu} \times 10^{-3}$) is kept the same with the previous examples for consistency.

F. Effect of the Virtual Shaft

Fig. 19 shows the frequency response when the damping parameter D_p of the VSM control of (48) is changed. The contingency for this case is a disconnection of the load at bus 6 at $t = 1$ s. Similar to the previous cases, the variation of

the control parameters affects the internal frequency of the converter to a greater extent than the one at the bus. The examples discussed in the next section show how this property can be utilized to improve the control of the converters.

G. Control Applications

This section illustrates the use of the converter *internal frequency* on control applications by means of two examples, one for GFL and one for GFM. While the frequency at the bus of the converter can be estimated (e.g., through a PLL), it is unclear whether it is the best signal one can use. For both GFL and GFM cases, a Primary Frequency Regulator (PFR) is added on top of the outer control layers described in the previous sections. Specifically, the PFR is added on top of the power controller (equation (37) and Fig. 3) for the GFL case and on top of the active power droop controller (equation (47) and Fig. 7 (a)) for the GFM case. The PFR is composed of a low-pass filter, a washout filter and a hard-limit [41]. The PFR modifies the active power reference p_{ref} by quantity Δp_{ref} based on an input frequency signal. The signals that are used for the comparison are the imaginary part of the CF at the converter bus and the imaginary part of the *internal* converter frequency as give by equations (7), (33) and (47). The comparison of the dynamic performance of the primary controllers based on the bus frequency and on the *internal* ones is the main objective of this section.

Fig. 20 shows the PFR input frequency signals after the contingency for the GFL case. Different type of signals and different values of PLL proportional gain K_p^{PLL} are used. In the zoomed-in version, it can be seen how the faster PLL ($K_p^{\text{PLL}} = 1$) matches the exact frequency after the initial transient. The slower PLLs introduce oscillations that remain for several seconds after the contingency. The impact of this control on the bus frequency is shown in Fig. 21. On the other hand, the faster the PLLs, the better the frequency response. This result is consistent with the case that uses the exact frequency signal. It can be concluded that the internal frequency of the converter can have similar results with the exact frequency at the bus when used for frequency control. This particularly useful for the cases where the exact signal is not available. However, careful tuning of the PLL parameters should be considered so that its bandwidth is suitably fast for the application while preventing undesired coupling with the dynamics of (weak) grids [42].

Fig. 22 shows the output signal of the PFR for the GFM case. The exact frequency at the bus is used as well as the internal frequency of the converter with different values of the active power droop gain m_p . It can be seen how the different input signals affects the controller operation until its output is saturated at $t = 3$ s. Fig. 23 shows the effect of the frequency control at the bus frequency. Results indicate that, if the droop gain is sufficiently large, the droop PFR outperforms the CF PFR for the first two seconds after the contingency.

H. Comparison between VSM and Synchronous Generator

This section illustrates how the CF can be used as a *metric* to directly compare the transient operation of a GFM converter

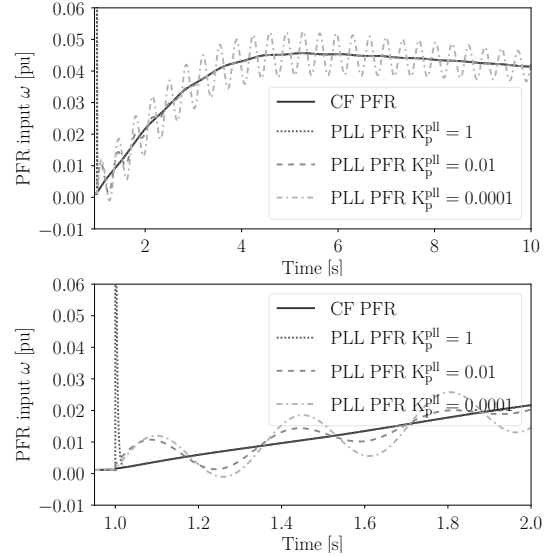


Fig. 20. Input signal (full and zoomed-in version) of the frequency control for the GFL case. Disconnection at $t = 1$ s of the load at bus 5 of the WSCC 9-bus system. The simulation is repeated for two types of input signal and different values of the PLL proportional gain K_p^{PLL} .

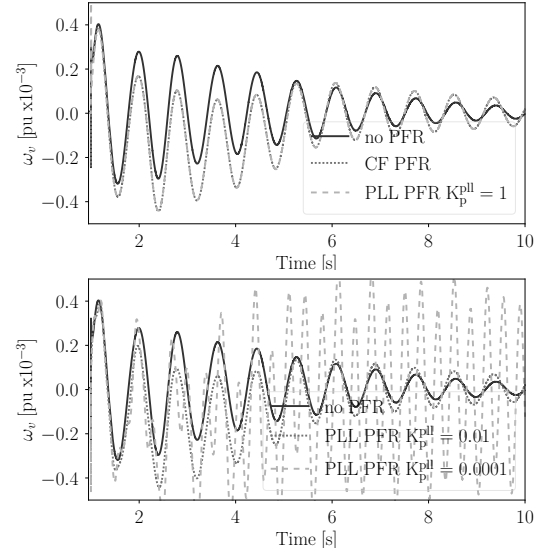


Fig. 21. Imaginary part of the CF as seen at bus 5 of the WSCC 9-bus system during the disconnection at $t = 1$ s of the load at bus 5. Application of frequency control for the GFL case. The simulation is repeated without frequency control, for two types of input signal and for different values of the PLL proportional gain K_p^{PLL} .

and a synchronous machine. For this case, the synchronous machine connected to bus 2 of the network, shown in Fig. 9, has been substituted with a VSM. The capacity of the VSM and the tuning of its control parameters are selected in such a way that the VSM operates similarly to the original synchronous machine. Finally, the same contingency considered in previous sections is applied also in this scenario.

Figures 24 and 25 show the real and imaginary parts, respectively, of the CF at bus 2, in the two scenarios, namely with synchronous machine and with VSM connected to the bus. An additional scenario is shown in these figures, i.e., a case for which the GFL converter at bus 5 is disconnected

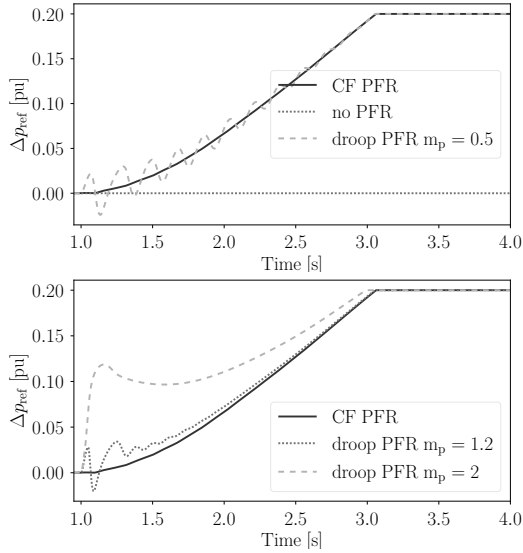


Fig. 22. Output signal of the frequency control for the GFM case. Disconnection at $t = 1$ s of the load at bus 5 of the WSCC 9-bus system. The simulation is repeated without frequency control, for two types of input signal and for different values of the active power droop parameter m_p .

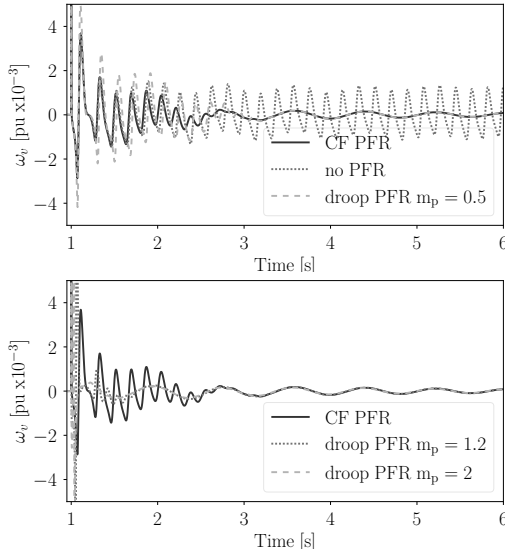


Fig. 23. Imaginary part of the CF as seen at bus 5 of the WSCC 9-bus system during the disconnection at $t = 1$ s of the load at bus 5. Application of frequency control for the GFM case. The simulation is repeated without frequency control, for two types of input signal and for different values of the active power droop parameter m_p .

and the VSM is the only converter in the system. It is shown that the control and implementation aspects of the VSM lead to different transient operation compared to a traditional synchronous generator. CF captures the discrepancies in the transient operation and can be used as a metric to directly compare them. Different trends for the system transient performance are identified through the use of the different quantities ρ_v , ω_v . Specifically, the magnitude of post-contingency oscillations of ρ_v is smaller for the synchronous machine while for ω_v , the use of the VSM results in smaller oscillations. The frequency response with the disconnected GFL converter is nearly identical with the case for which it

is connected. This fact highlights that the interaction between the different converter control configurations does not affect CF significantly.

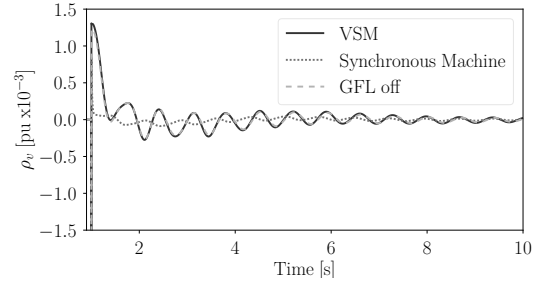


Fig. 24. Real part of the CF as seen at bus 2 of the WSCC 9-bus system during the disconnection at $t = 1$ s of the load at bus 5. The simulation is repeated with a synchronous generator connected to bus 2, a VSM substituting the synchronous generator and the GFL converter at bus 5 disconnected.

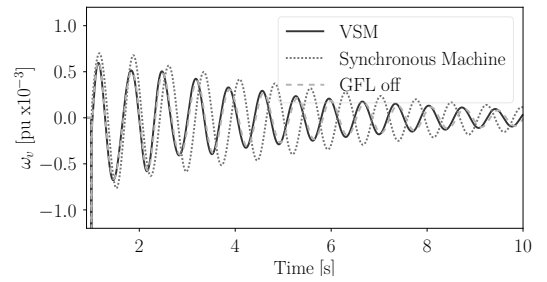


Fig. 25. Imaginary part of the CF as seen at bus 2 of the WSCC 9-bus system during the disconnection at $t = 1$ s of the load at bus 5. The simulation is repeated with a synchronous generator connected to bus 2, a VSM substituting the synchronous generator and the GFL converter at bus 5 disconnected.

VII. CONCLUSION

In this paper, the concept of CF is utilized to develop a taxonomy of different power-converter control schemes. Both GFL and GFM control configurations are studied and their effect on the local frequency is analytically derived. Theoretical results are complemented with a case study based on a modified model of the WSCC 9-bus system, where the derived analytical formulations are used for control applications for both GFLs and GFMs.

Results show that CF approach decouples the contribution on the local frequency of each sub-controller and identifies critical control parameters. For all converters, the current controller is shown to represent a constant translation of the real part of the CF while the synchronization control, regardless of its type, affects the imaginary part. For GFL configurations, the PLL parameters are shown to have the largest impact on the local frequency. For GFM, active power droop parameter as well as VSM damping parameter are shown to affect the frequency response after a contingency. For the GFL control application case, the internal frequency of the converter, used as an input to a PFR, achieves the same frequency response with the exact frequency measurement, provided that the PLL is sufficiently fast. For the GFM case, the internal frequency of the controller achieves a better transient response than the exact frequency.

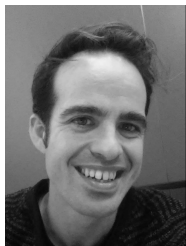
In this work, the dynamic effect of conventional controllers on the frequency at their point of connection was presented and classified. Future work will focus on extending the use of the calculated internal frequencies of the converters for control applications. The potential of using non-conventional controllers based on CF or controllers based on non-conventional input signals, such as the real part and the magnitude of the CF, will also be further explored. Finally, the effect on CF of multiple converters, their dynamic interaction and the impact of this interaction on converter frequency control will also be studied.

REFERENCES

- [1] IEEE Power System Stability Controls Subcommittee, "Contribution to bulk system control and stability by distributed energy resources connected at distribution network," IEEE, Tech. Rep. PES-TR22, 2017.
- [2] A. Tayyebi, D. Groß, A. Anta, F. Kupzog, and F. Dörfler, "Frequency stability of synchronous machines and grid-forming power converters," *IEEE JESTPE*, vol. 8, no. 2, pp. 1004–1018, 2020.
- [3] R. Rosso, X. Wang, M. Liserre, X. Lu, and S. Engelken, "Grid-forming converters: Control approaches, grid-synchronization, and future trends – A review," *IEEE Open J. of Industry Apps*, vol. 2, pp. 93–109, 2021.
- [4] X. Wang, M. G. Taul, H. Wu, Y. Liao, F. Blaabjerg, and L. Harnefors, "Grid-synchronization stability of converter-based resources – An overview," *IEEE Open J. of Industry Apps*, vol. 1, pp. 115–134, 2020.
- [5] J. Rocabert, A. Luna, F. Blaabjerg, and P. Rodríguez, "Control of power converters in ac microgrids," *IEEE Trans. on Power Electronics*, vol. 27, no. 11, pp. 4734–4749, 2012.
- [6] Y. Li, Y. Gu, and T. Green, "Revisiting grid-forming and grid-following inverters: A duality theory," *IEEE Trans. on Power Systems*, 2022.
- [7] T. Wu, Q. Jiang, M. Huang, and X. Xie, "Synchronization stability of grid-following converters governed by saturation nonlinearities," *IEEE Trans. on Power Systems*, 2022.
- [8] J. Chen, M. Liu, H. Geng, T. O'Donnell, and F. Milano, "Impact of pll frequency limiter on synchronization stability of grid feeding converter," *IEEE Trans. on Power Systems*, vol. 37, no. 3, pp. 2487–2490, 2022.
- [9] N. Pogaku, M. Prodanovic, and T. C. Green, "Modeling, analysis and testing of autonomous operation of an inverter-based microgrid," *IEEE Trans. on Power Electronics*, vol. 22, no. 2, pp. 613–625, 2007.
- [10] D. P. Moran-Rio, J. Roldán-Pérez, M. Prodanović, and A. García-Cerrada, "Influence of the phase-locked loop on the design of microgrids formed by diesel generators and grid-forming converters," *IEEE Trans. on Power Electronics*, vol. 37, no. 5, pp. 5122–5137, 2021.
- [11] Q.-C. Zhong and G. Weiss, "Synchroverters: Inverters that mimic synchronous generators," *IEEE Trans. on Ind. Electronics*, vol. 58, no. 4, pp. 1259–1267, 2010.
- [12] J. Roldán-Pérez, A. Rodríguez-Cabero, and M. Prodanovic, "Design and analysis of virtual synchronous machines in inductive and resistive weak grids," *IEEE Trans. on En. Conv.*, vol. 34, no. 4, pp. 1818–1828, 2019.
- [13] A. González-Cajigas, J. Roldán-Pérez, and E. J. Bueno, "Design and analysis of parallel-connected grid-forming virtual synchronous machines for island and grid-connected applications," *IEEE Trans. on Power Electronics*, vol. 37, no. 5, pp. 5107–5121, 2021.
- [14] S. D'Arco and J. A. Suul, "Virtual synchronous machines—classification of implementations and analysis of equivalence to droop controllers for microgrids," in *2013 IEEE Grenoble Conference*. IEEE, 2013, pp. 1–7.
- [15] S. D'Arco, J. A. Suul, and O. B. Fosfo, "A virtual synchronous machine implementation for distributed control of power converters in smartgrids," *Elec. Power Sys. Research*, vol. 122, pp. 180–197, 2015.
- [16] H. Kirkham, W. Dickerson, and A. Phadke, "Defining power system frequency," in *IEEE PES General Meeting*. IEEE, 2018, pp. 1–5.
- [17] F. Milano and Á. Ortega, "Frequency divider," *IEEE Trans. on Power Systems*, vol. 32, no. 2, pp. 1493–1501, 2016.
- [18] F. Milano, "Complex frequency," *IEEE Trans. on Power Systems*, vol. 37, no. 2, pp. 1230–1240, 2022.
- [19] IEC/IEEE 60255-118-1, "IEEE/IEC international standard—measuring relays and protection equipment—part 118-1: Synchrophasor for power systems—measurements," 2018.
- [20] F. Milano, G. Tzounas, I. Dassios, M. A. A. Murad, and T. Kërçi, "Using differential geometry to revisit the paradoxes of the instantaneous frequency," *IEEE Open Access Journal of Power and Energy*, vol. 9, pp. 501–513, 2022.
- [21] L. Cohen, *Time-Frequency Analysis: Theory and Applications*. Upper Saddle River, NJ: Prentice-Hall Signal Processing, 1995.
- [22] F. Milano, "A geometrical interpretation of frequency," *IEEE Trans. on Power Systems*, vol. 37, no. 1, pp. 816–819, 2022.
- [23] F. Milano, G. Tzounas, I. Dassios, and T. Kërçi, "Applications of the Frenet frame to electric circuits," *IEEE Transactions on Circuits and Systems I: Regular Papers*, vol. 69, no. 4, pp. 1668–1680, 2022.
- [24] W. Zhong, G. Tzounas, M. Liu, and F. Milano, "On-line inertia estimation of virtual power plants," *Elec. Power Sys. Research*, vol. 212, p. 108336, 2022.
- [25] M. Colombino, D. Groß, J.-S. Brouillon, and F. Dörfler, "Global phase and magnitude synchronization of coupled oscillators with application to the control of grid-forming power inverters," *IEEE Trans. on Automatic Control*, vol. 64, no. 11, pp. 4496–4511, 2019.
- [26] X. He, V. Häberle, and F. Dörfler, "Complex-frequency synchronization of converter-based power systems," *arXiv:2208.13860*, 2022.
- [27] W. Zhong, G. Tzounas, and F. Milano, "Improving the power system dynamic response through a combined voltage-frequency control of distributed energy resources," *IEEE Transactions on Power Systems*, vol. 37, no. 6, pp. 4375–4384, 2022.
- [28] A. Yazdani and R. Iravani, *Voltage-sourced converters in power systems: modeling, control, and applications*. John Wiley & Sons, 2010.
- [29] Á. Ortega and F. Milano, "Comparison of different PLL implementations for frequency estimation and control," in *Int. Conf. on Harmonics and Quality of Power (ICHQP)*. IEEE, 2018, pp. 1–6.
- [30] Z. Ali, N. Christofides, L. Hadjidemetriou, E. Kyriakides, Y. Yang, and F. Blaabjerg, "Three-phase phase-locked loop synchronization algorithms for grid-connected renewable energy systems: A review," *Renewable and Sustainable Energy Reviews*, vol. 90, pp. 434–452, 2018.
- [31] R. Teodorescu, M. Liserre, and P. Rodríguez, *Grid converters for photovoltaic and wind power systems*. John Wiley & Sons, 2011.
- [32] D. Moutevelis, J. Roldan-Perez, and M. Prodanovic, "Virtual admittance control for providing voltage support using converter interfaced generation," in *IEEE PES ISGT Europe*. IEEE, 2021, pp. 01–06.
- [33] J. Yang, K. T. Chi, M. Huang, and D. Liu, "Bifurcations of grid-following rectifiers and routes to voltage instability in weak ac grids," *IEEE Trans. on Power Systems*, 2022.
- [34] M. Huang, Y. Peng, K. T. Chi, Y. Liu, J. Sun, and X. Zha, "Bifurcation and large-signal stability analysis of three-phase voltage source converter under grid voltage dips," *IEEE Trans. on Power Electronics*, vol. 32, no. 11, pp. 8868–8879, 2017.
- [35] J. C. Vásquez, R. A. Mastromauro, J. M. Guerrero, and M. Liserre, "Voltage support provided by a droop-controlled multifunctional inverter," *IEEE Trans. on Ind. El.*, vol. 56, no. 11, pp. 4510–4519, 2009.
- [36] Z. Yang, R. Ma, S. Cheng, and M. Zhan, "Nonlinear modeling and analysis of grid-connected voltage-source converters under voltage dips," *IEEE JESTPE*, vol. 8, no. 4, pp. 3281–3292, 2020.
- [37] Á. Ortega and F. Milano, "Generalized model of VSC-based energy storage systems for transient stability analysis," *IEEE Trans. on Power Systems*, vol. 31, no. 5, pp. 3369–3380, 2015.
- [38] F. Milano, "A Python-based software tool for power system analysis," in *IEEE PES General Meeting*. IEEE, 2013, pp. 1–5.
- [39] —, *Power system modelling and scripting*. Springer Science & Business Media, 2010.
- [40] P. S. Kundur and O. P. Malik, *Power system stability and control*. McGraw-Hill Education, 2022.
- [41] F. Sanniti, G. Tzounas, R. Benato, and F. Milano, "Curvature-based control for low-inertia systems," *IEEE Trans. on Power Systems*, 2022.
- [42] B. Wen, D. Boroyevich, R. Burgos, P. Mattavelli, and Z. Shen, "Analysis of d-q small-signal impedance of grid-tied inverters," *IEEE Trans. on Power Electronics*, vol. 31, no. 1, pp. 675–687, 2016.



Dionysios Moutevelis received the M.Eng. degree in Electrical and Computer Engineering from the National Technical University of Athens, Greece in 2017. In 2019 he joined IMDEA Energy Institute, Madrid, Spain where he is currently working as a pre-doctoral researcher. From May to August 2022 he was with University College Dublin, Ireland, as a visiting researcher. His research interests include stability analysis of power systems and power converter control.



Javier Roldán-Pérez (S'12-M'14) received a B.S. degree in industrial engineering, a M.S. degree in electronics and control systems, a M.S. degree in system modeling, and a Ph.D. degree in power electronics, all from Comillas Pontifical University, Madrid, in 2009, 2010, 2011, and 2015, respectively. From 2010 to 2015, he was with the Institute for Research in Technology (IIT), Comillas University. In 2014, he was a visiting Ph.D. student at the Department of Energy Technology, Aalborg University, Denmark. From 2015 to 2016 he was with the Electric and Control Systems Department at Norvento Energía Distribuida. In September 2016 he joined the Electrical Systems Unit at IMDEA Energy Institute. In 2018, he did a research stay at SINTEF Energy Research, Trondheim. His research topics are the integration of renewable energies, microgrids, and power electronics applications.



Federico Milano (F'16) received from the Univ. of Genoa, Italy, the M.E. and Ph.D. in Electrical Engineering in 1999 and 2003, respectively. From 2001 to 2002 he was with the University of Waterloo, Canada, as a Visiting Scholar. From 2003 to 2013, he was with the University of Castilla-La Mancha, Spain. In 2013, he joined the University College Dublin, Ireland, where he is currently a full professor. He is also Chair of the IEEE Power System Stability Controls Subcommittee, IET Fellow, IEEE PES Distinguished Lecturer, Chair of the Technical Programme Committee of the PSCC 2024, Senior Editor of the IEEE Transactions on Power Systems, Member of the Cigre Irish National Committee, and Co-Editor in Chief of the IET Generation, Transmission & Distribution. His research interests include power system modeling, control and stability analysis.



Milan Prodanovic (Member, IEEE) received the B.Sc. degree in electrical engineering from the University of Belgrade, Belgrade, Serbia, in 1996 and the Ph.D. degree in electric and electronic engineering from Imperial College, London, U.K., in 2004. From 1997 to 1999, he was with GVS engineering company, Serbia, developing UPS systems. From 1999 until 2010, he was a Research Associate in electrical and electronic engineering with Imperial College. He is currently a Senior Researcher and Head of the Electrical Systems Unit, Institute IMDEA Energy, Madrid, Spain. He authored a number of highly cited articles and is the holder of three patents. His research interests include design and control of power electronics interfaces for distributed generation, microgrids stability and control, and active management of distribution networks.